Hindawi
Geofluids
Volume 2022, Article ID 1378563, 16 pages
https://doi.org/10.1155/2022/1378563

Research Article

Occurrence Characteristics and Threshold Pore Throat Radius of Movable Fluids for Dolomite Intercrystalline Pores of Lacustrine Carbonate Rocks

Shiming Zhang,[1,2] **Xiaojun Zhang**,[1,2] **Tingjing Zhang**,[1,2] **Yongxian Zheng**,[3] **Jun Cui**,[3] **Juerong Fu**,[1,2] **Chao Wang**,[1,2] **and Xiaofeng Yu**[1,2]

[1]*Northwest Branch of Research Institute of Petroleum Exploration and Development, CNPC, Lanzhou 730020, China*
[2]*Key Laboratory of Reservoir Characterization, CNPC, Lanzhou 730020, China*
[3]*Research Institute of Petroleum Exploration and Development, Qinghai Oilfield, CNPC, Dunhuang 736202, China*

Correspondence should be addressed to Xiaojun Zhang; xj_zhang@petrochina.com.cn

Received 30 May 2022; Revised 23 July 2022; Accepted 1 September 2022; Published 23 September 2022

Academic Editor: Dazhong Ren

The reservoir evaluation and classification are restrained by the progress of research on the pore structure and fluid occurrence in dolomite intercrystalline pores of the Paleogene lacustrine carbonate rock in the western Qaidam Basin. The experimental method adopted to investigate the fluid occurrence of the lacustrine carbonate rock in the study area can be used as a reference for studying tight reservoirs. By integrating technical approaches such as the thin-section petrographic analysis, SEM, electron probe, mercury injection test, and NMR test, this research studies the petrology, pore type and distribution, and pore structure of the reservoir. Moreover, the pore fluid distribution and threshold pore throat radius for the distribution of movable fluids are investigated by integrating the centrifuging treatment and NMR characterization. Results show that pores of samples in the study area are dolomite intercrystalline pores, intercrystalline dissolved pores, framework dissolved pores of algal limestone (dolostone), dissolved pores of saline minerals, and interlayer fractures, among which dolomite intercrystalline pores and intercrystalline dissolved pores are found with the highest proportions (60%). The dolomite intercrystalline pores and intercrystalline dissolved pores are nano-micropore throats with a narrow distribution. Their capillary pressure curve is characterized by a high plateau and negative skewness, while the NMR relaxation time spectrum is left-skewed and presents higher bond water saturation (over 65%). For intercrystalline pores and intercrystalline dissolved pores, the main storage space for movable fluids is provided by small and medium pores (corresponding to the NMR relaxation time of 1–10 ms and 10–100 ms, respectively), and the experimentally determined threshold pore throat radius for movable fluids is 47 nm. The reservoir is hydrophilic and therefore movable fluids mainly occur in the centers of pores. The samples with higher proportions of coarse pores and pore connectivity are associated with higher proportions of movable fluids. Our analysis shows the dolomite intercrystalline pore has a certain storage capacity and yet inferior connectivity; the proportion of movable fluids that can effectively flow is key to evaluating the effectiveness of reservoirs with dolomite intercrystalline pores.

1. Introduction

The lacustrine carbonate rock, often associated with high capacities of hydrocarbon generation and storage, develops extensively across continental petroliferous basins. Therefore, it is considered an important target for exploring tight oil [1, 2], and numerous lacustrine carbonate oil and gas reservoirs have been discovered globally [3–6]. Lacustrine carbonate sediments mainly occur in the shallow-water area of the lacustrine basin. They are affected not only by the sedimentary environment of terrigenous clasts but also that of evaporate. They are subjected to the control of variations of the paleo-climate, paleo-hydrodynamics, and paleo-water condition, and mainly found with the development

of rock types such as the bioclastic limestone, algal limestone, muddy limestone, and dolostone [7–10]. The pores of the lacustrine carbonate rock are seen with the predominance of residual primary intergranular pores (residual organic-framework pores after cementation and residual intergranular pores), secondary dissolved pores (dissolved pores of feldspar, carbonates, and lithics), intercrystalline pores (occurring among micritic dolomite or other authigenic minerals with small pore throat radii and in large quantities), and fractures (interlayer and structural fractures). The porosity of the lacustrine carbonate rock lies in a relatively wide range, typically from 3% to 25%, averaging 10%. In most cases, permeability is low, often below 0.1 mD, which represents a typical tight reservoir [11–13].

The study area is the lacustrine carbonate rock of the Palaeogene Lower Ganchaigou Formation in the western Qaidam Basin. During the Palaeogene, the West Qaidam is found with the largest coverage of the lake, and the lacustrine carbonate rock peaks in its development. The carbonate rocks, represented by the algal limestone, marlstone, and grainstone, have been successively discovered in the Hongliuquan-Yuejin area of the Southwest Qaidam and the Xiaoliangshan-Nanyishan area of the Northwest Qaidam [14–16], and the mixed deposition of carbonate rocks with mudstone, terrigenous clastic particles, and saline minerals have been identified in the Yingxi area [17]. Ganchaigou, Qigequan, Honggouzi, Xianshuiquan, Nanyishan, Dawusi, Mangnai, Jianshegou, Youshashan, etc. are all found with the distribution of carbonate rocks [18, 19]. Over recent years, numerous researchers have investigated the sedimentary evolution, lithological association, genesis, and formation mechanisms of high-quality reservoirs of such carbonate rocks [20–24]; moreover, for the first time the nano-scale dolomite intercrystalline pore is discovered and the pore throat distribution characteristics and control factors of reservoirs presenting intercrystalline pores are analyzed [25, 26]. However, the pore structure of the dolomite intercrystalline pore in the lacustrine carbonate rock and the effectiveness of fluids contained in such pores are less studied. In addition, the current research on the pore structure is mostly carried out in an imaging or fluid injection approach, which seldom analyzes the fluid distribution in the pore structure of interest [27–31]. Based on the thin section observation, argon ion polishing-assisted scanning electron microscopy (SEM), high-pressure mercury intrusion, and nuclear magnetic resonance (NMR) test, this research experimentally investigates the pore structure characteristics of the dolomite intercrystalline pore of the lacustrine carbonate rock. Furthermore, the NMR test is integrated with the centrifuge treatment to study the fluid distribution in the intercrystalline pore and the threshold pore throat radius for movable fluids is experimentally determined. The findings of this research provide the scientific basis for evaluating the storage capacity of intercrystalline pores of the lacustrine carbonate rock. This study combines the fluid occurrence characteristics with the distribution of pore throats, and studies the proportion of movable fluids in pores of different scales, which is of great significance for the study of microscopic characterization of tight reservoirs, On the other hand, the determination of threshold pore throat radius for movable fluids is of great significance to evaluate the effectiveness of tight reservoirs.

2. Geological Setting

The West Qaidam (the western Qaidam Basin) is structurally located in the Gasikule fault depression sub-zone of the Western Depression belt. The formations encountered during drilling are mainly the Upper Youshashan Formation (N_2^2), Lower Youshashan Formation (N_2^1), Upper Ganchaigou Formation (N_1) and the Upper Member of the Lower Ganchaigou Formation (E_3^2), etc. The West Qaidam represents a typical intermountain-enclosed plateau salinized lake basin that experiences the Palaeogene maximum flooding and is underfilled for a prolonged period. The piedmont of the Northwest Qadiam develops the fan delta, sublacustrine fan, and lacustrine deposition, while the Southwest Qaidam is found with the braided river delta and shore-shallow lake beach bar. The Yingxiongling area of the West Qaidam is the Palaeogene deposition center, where the carbonate deposition of the semi-deep lacustrine facies occurs (Figure 1). The Upper Member of the Palaeogene Lower Ganchaigou Formation (E_3^2) is the key exploration target. This layer features a thickness of over 2200 m and complicated lithology. Vertically, it is mainly composed of carbonate rocks, mudstone, siltstone, and some gypsum and halite, with carbonate rocks interbedding with mudstone and siltstone, or banded or uniform dispersion of fine clastic particles in carbonate rocks (Figure 1). In a plane view, the lithology also varies greatly from the delta facies to the semi-deep lake facies. Specifically, the fan delta mainly consists of sandstone and mudstone; from the shore-shallow lake to the slope the lithology is dominated by the mixed deposition of clastic and carbonate rocks (mostly blocky mixed rock with similar content of carbonates and clasts that are thoroughly mixed; besides the mixed rock, the transitional lithology between carbonate rocks and mudstone is also often identified); the shallow lake facies is found with the laminar algal limestone (dolostone) and grainstone; the semi-deep lake is the main deposition area for lacustrine carbonate rocks. The lacustrine deposition is characterized by the relatively shallow depth and intensive fluctuation of waters. The corresponding carbonate rock is thin and has complex composition. The lithology of the lacustrine deposition mainly includes carbonate rocks and mudstone. The turbidite occurs at the bottom of the lake basin, while the algal limestone (dolostone) and grainstone come into being in the uplift area of the lake basin; during the late stage of the deposition, laminated halite and gypsum occur.

3. Methodology

The core samples of the E_3^2 lacustrine carbonate rock are collected from the drilled wells in the West Qaidam for tests and analysis. According to previous studies on the sedimentary facies and reservoir characteristics of the Lower Ganchaigou Formation in the study area and also the core observation, the core samples of 10 wells of the Yuejin,

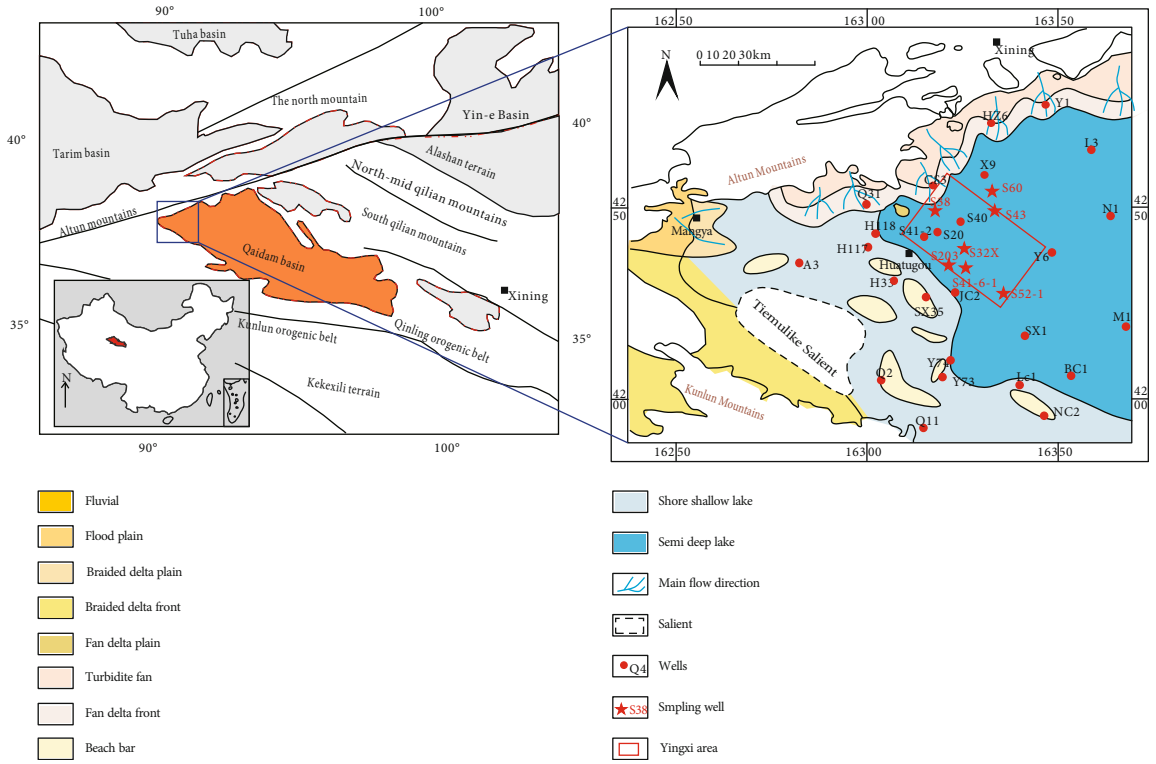

Figure 1: Sedimentary environment and the location of Yingxi area, western Qaidam Basin.

Yingxi, and Ganchaigou areas in the West Qaidam are used for this research. The samples are generally grey and dark grey mixed carbonate rocks, mostly with blocky and laminated textures. The main rock composition is the micritic dolomite and micritic calcite, associated with the laminated, banded, or crumby distribution of silty clastic particles and breccia and masses of saline minerals. The samples are mixed of siliciclastic and carbonate, which mainly include halite, glauberite, anhydrite, dolomite, calcite, pyrite, clastic, and clay (Table 1).

By the rock fabric and composition, the carbonate rock in the study area can be divided into the following types. Clay-bearing limestone (dolostone); gypseous limestone (dolostone) featuring the snowflake, rhombus, or crumby distribution of gypsum in carbonate rocks (besides gypsum, saline minerals also include some halite, mirabilite, and celestite); algal limestone (dolostone), laminated or crumby; grainstone (granular dolostone), of which grains are micritic calcite, micritic dolomite, or argillaceous pellets and the matrix is mainly of the micritic carbonate rock.

The experimental methods adopted to investigate the rock mineral composition, pore type, structure, and fluid distribution are presented below. The rock mineral composition is analyzed using the thin-section petrographic analysis, X-ray diffraction mineral composition analysis, and electron probe. The thin section petrographic analysis is performed using a Zeiss microscope. The XRD analysis adopts the Empyrean X-ray diffractometer (PANalytical, Netherlands). Two grams of the core sample are ground to powder all smaller than 40 μm and subsequently the sample power is used to prepare the test specimen. The working voltage is 40 kV, the working current is 40 mA, and the scan rate is 2° (2θ)/min. The electron probe test is done using the Shimadzu 1720 Electron Probe Microanalyzer, of which the working voltage is 15 kV, the current intensity is 25 μA, and the beam size is less than 5 μm.

The pore characteristics are observed via the casting thin-section microscopy and SEM of argon-ion polished specimens. The field-emission environmental SEM (FEI Quanta 450 FEG) is used, with the working voltage of 20 kV and the incident electron beam of 0.3–0.4 nA. Concerning the pore-structure of samples, the physical properties of reservoirs are determined using the automated porosimeter-permeameter and the high-pressure mercury intrusion test is performed to characterize the pore throat size distribution. The porosity-permeability measurement under the confining pressure is performed using the CMS-300 porosimeter-permeameter (Core Laboratories, the US), which can measure porosity and permeability under the pressure of 800–12000 psi, with the precision of 10^{-4}. The high-pressure mercury intrusion test is implemented using the AutoPore IV 9500 automatic mercury injection porosimeter (Micromeritics, the US), which measures pore throats from 3 nm to 1000 μm and features the volumetric precision at 0.0001 mL.

The samples are saturated with the simulated formation water and put through the NMR test to study the overall fluid distribution and pore structure of the samples. The NMR test is based on the fact that hydrogen nuclei of fluids are polarized in a magnetic field; the nuclear magnetic resonance occurs when the sample is subjected to a stable external magnetic field, and the NMR signal attenuates

Table 1: XRD analysis results of mineral compositions.

Well	Depth(m)	Percentage content (%)							
		Halite	Anhydrite	Glauberite	Calcite	Dolomite	Pyrite	Clastic	Clay
S32X	4055.8	0	5.4	0	8.2	50.6	6.3	6.4	5.1
S32X	4062.5	0	25.7	0	14	36.1	5.1	6.3	9.3
S32X	4072.74	0.4	2.2	0	21.3	56.2	0	11.5	5.2
S32X	4090.9	0	31.8	0	4.4	43.9	0	12.1	7.7
S32X	4091.6	0	11.2	4.7	9.3	52.6	0	7.3	7.9
S32X	4093.1	0	10.4	0	12.4	46.6	0	13.4	17.2
S32X	4096.86	0	0.6	0	18.4	45.4	4.7	13.5	13.6
S32X	4097.87	0	13	0	7	64.5	0	6.2	4.1
S32X	4098.57	0	34.2	0	2.8	49.6	0	8.2	5.2
S32X	4123.35	0	12.8	0	33.4	36.7	3.3	7.5	6.3
S32X	4125.99	0	6.7	0	7.2	65.7	0	3.9	7.8
S32X	4126.49	0	7.1	0	9.6	47	5.1	7.3	13.3
S32X	4127.93	0	1.1	0	11.6	64.4	0	10	12.8
S32X	4129.03	0	0.9	0	14.9	49.2	2.8	12.3	14.7
S32X	4135.48	0	0.7	0	12.6	68.1	0	6.3	5.7
S32X	4136.08	0	0.9	0	9	61.6	6.8	11.5	9.7
S32X	4139.63	0	11.7	0	16.1	55.6	0	6.2	4.9
S32X	4140.25	0	10.4	0	15.1	50.2	0	6.8	13.2
S32X	4141.7	0	5.6	0	12.5	47.5	0	7.8	10.2
S32X	4142.3	0.6	7	0	9.9	64.3	0	4.9	4.4
S32X	4143.8	0	1	0	9.4	56.4	0	10	16.7
S38	3146.49	1.6	0	11.3	6.4	52.5	0	6.9	21.3
S38	3147.01	1.7	1.1	0	9	39.1	8	13.5	27.8
S43	3914.43	0	1	0	26.1	50.5	6.4	16	0
S43	3925.95	0	0	0	20.3	53.4	5.4	18.4	0
S43	3926.12	0	0	0	24.5	57.4	0	9.2	0
S43	3926.35	0	0.9	0	30.4	51.3	0	14.3	0
S43	3926.5	0	0.8	0	30.2	42.8	0	19.9	0
S43	3926.66	0	0.9	0	20.8	43.5	5.3	29.5	0
S43	3927.1	0	1	0	9	53.2	4.1	17.5	15.3
S43	3927.18	0	0.8	0	22.9	56.1	0	20.3	0
S43	3927.68	0	0	0	34.1	43.4	3.8	18.7	0

exponentially after the magnetic field is revoked. The signal attenuation process can be mathematically converted into the NMR relaxation time spectrum for expression. The NMR signal attenuation is the superimposition of signal attenuation of fluids in pores, and the attenuation time prolongs with a larger pore throat [32–35]. In addition, as the NMR relaxation mechanism suggests, the transverse relaxation time approximately equals the surface relaxation time and the surface relaxation time is positively correlated with the specific surface area of the sample [36–38], which is related to the pore radius. Hence, a linear correlation exists between the T_2 relaxation time and the pore radius r and the NMR T_2 relaxation time can be converted to the pore throat radius as soon as the conversion coefficient C is determined ($r = C^* T_2$). Different values of C are reported in different studies. In a mathematical approach based on the maximum correlation principle, the C value of mudstone and sandstone with different degrees of weathering is determined to be 0.31–0.35 μm/ms [39]. By fitting the cumulative pore radius distribution based on the NMR T_2 spectrum with that measured by the low-temperature low-pressure nitrogen adsorption test, Gong et al. determine that the C value of the shale of the Longmaxi Formation in Sichuan, China, shall be 0.02 μm/ms [40]. The tight lacustrine carbonate rock is similar to the Longmaxi Formation shale, in terms of the rock composition (they both consists of three components, namely, carbonate rocks, clays, and clastic particles) and pore size distribution (a unimodal-bimodal pore throat distribution with pore throat radii mostly below 100 nm). Accordingly, the value of the conversion coefficient C is set as 0.02 μm/ms in this research.

The difficulty in effective migration for fluids contained in pores is evaluated via the repeated centrifuging-NMR test, which measures the relative proportion of movable fluids

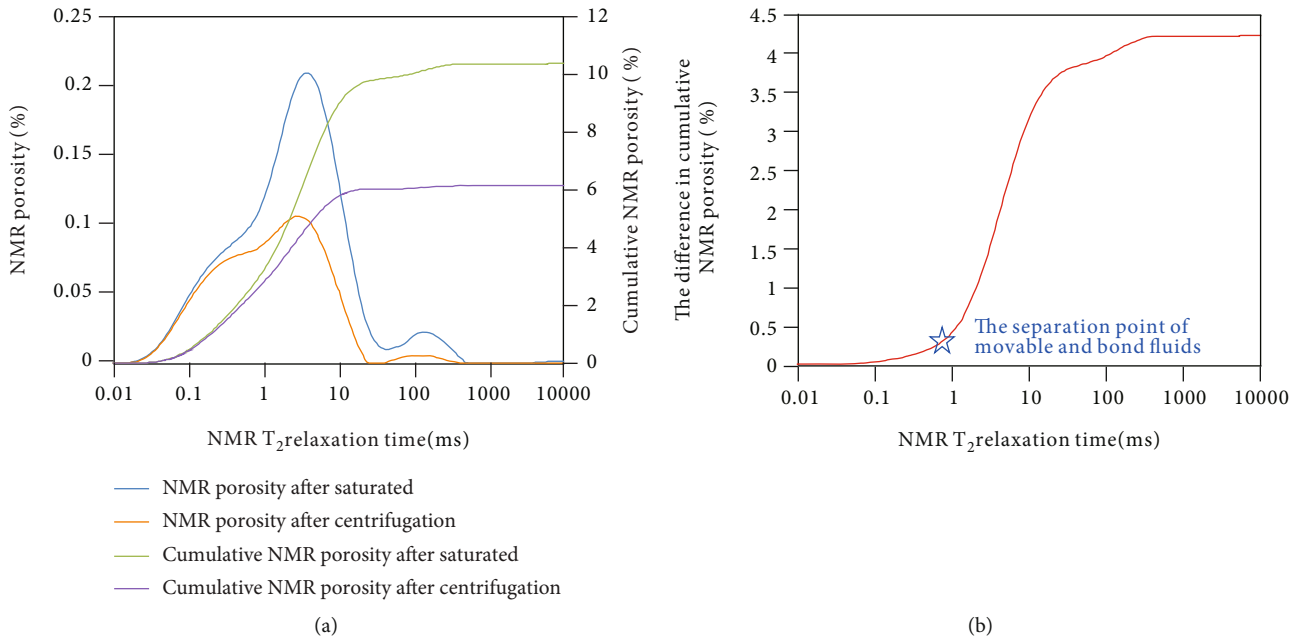

Figure 2: The separation point of the moveable fluid and the irreducible fluids.

and determines the threshold pore throat radius of movable fluids [40–42]. First, the saturated core sample is put through the high-speed centrifuge, which resembles a gas flooding process. As the rotation speed of centrifuging grows, the pore throat radius, corresponding to movable fluids displaced by air, declines. Ultimately, the pores are associated with only bond fluids after the centrifuging treatment. The T_2 relaxation spectra before and after each centrifuging are compared to investigate the movable fluid variation in the T_2 relaxation time spectrum. If the area enclosed by the movable fluid envelope and the horizontal axis shrinks after centrifuging, it means that there are still movable fluids after this centrifuging, and then, one shall increase the centrifuging rotation speed for the centrifuging-NMR test. The test is repeated until the envelope area of movable fluids remains the same after centrifuging, and it is considered that only bond fluids exist in the sample at this moment.

The difference of the T_2 relaxation time cumulative curves between the initial saturated sample (representing movable and bond fluids) and the ultimate postcentrifuging sample (representing bond fluids) versus the relaxation time is triple-segmented. The segments on the two sides present slow slopes, while the central curve segment is steep (Figures 2(a) and 2(b)). The left segment of lower relaxation time corresponds to smaller pore throat radii, which indicates that no movable fluids are present in micropore throats (the curve difference is zero or an extremely low positive value). The curve difference grows with the increasing relaxation time in the central segment, which demonstrates that movable fluids start to separate in small-medium pores. The right segment presents relatively stable high values, implying that in large pores movable fluids have already been separated from bond fluids. The inflection point between the left and central segments of the T_2 relaxation time difference versus relaxation time represents the separation point of movable and bond fluids (Figures 2(a) and 2(b)). The horizontal axis value at the separation point is the relaxation time value for the separation of movable and bond fluids, which can be converted to the corresponding pore throat radius at the separation point via the conversion equation ($r = C^* T_2$). The computed radius is considered the threshold pore throat radius for the movable fluid distribution (in other words, the minimal pore throat radius below which fluids cannot migrate).

The NMR test is performed using the MesoMR23-60H-I NMR imaging analysis system. The test echo spacing is 0.1 ms; the waiting time is 5000 ms; the echo number, 6000; the scan times is 64. The test procedure is summarized below. First, the core cylinder with a diameter of 25 mm is treated to remove oil and dried, after which it is placed in a vacuum-pressurization saturation instrument at 20 MPa for 72 hours for saturation with the simulated formation water. The simulated formation water (45000 mg/L $CaCl_2$ solutions) is prepared, according to the salinity of the actual formation water. Subsequently, the NMR T_2 spectrum measurement and imaging are performed for the saturated sample. Then, the saturated sample is centrifuged using the high-speed centrifuge for 120 min, after which the NMR fluid imaging and relaxation time measurement are performed. The centrifuging treatment is done four times and the rotation speed grows for each time (the rotation speed at 800 rpm corresponds to the centrifugal force of 0.144 MPa; 1600 rpm, to 0.288 MPa; 4000 rpm, to 0.576 MPa; 8000 rpm, to 1.44 MPa).

4. Experiment Results

4.1. Pore Structure Characteristics of Intercrystalline Pores

4.1.1. Pore Throat Types. The pore types analyzed in this research are nano-microintercrystalline pores and intercrystalline dissolved pores (accounting for 60% of total pores) of

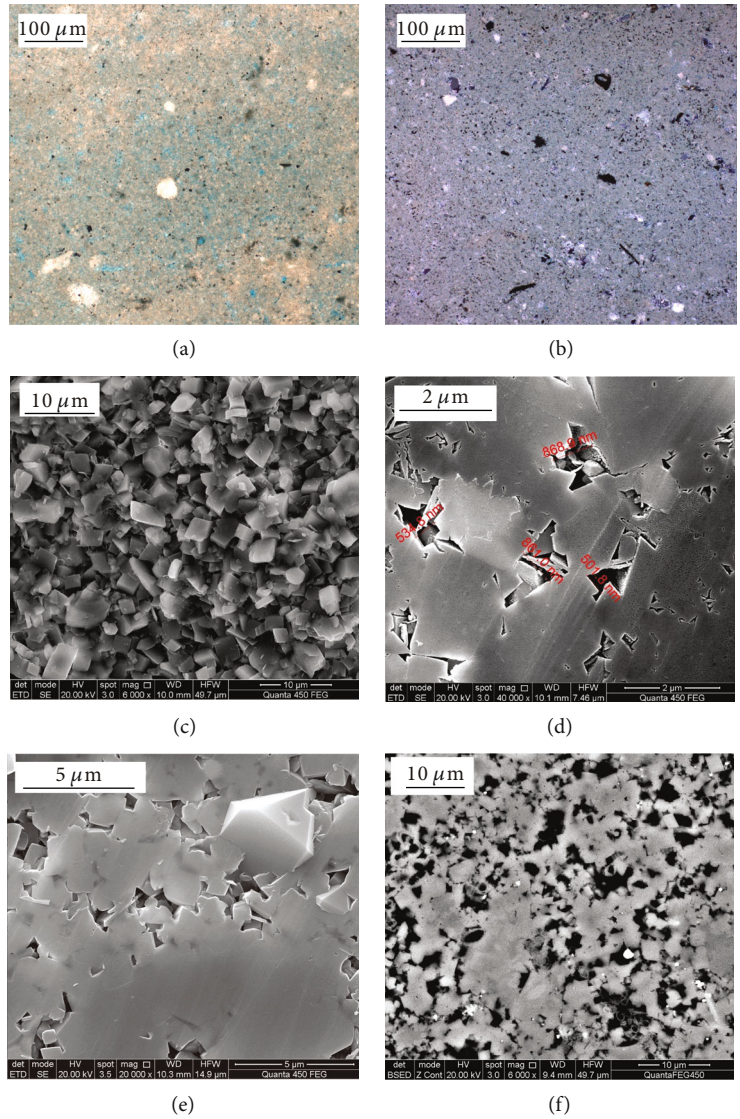

Figure 3: Images of intercrystalline pores and intercrystalline dissolve pores. (a) 3294.2 m, image of intercrystalline dissolve pores of dolomite, casting thin-section image. (b) 3145.86 m, image of intercrystalline pores of dolomite, casting thin-section image. (c) 3780.90 m, image of intercrystalline pores of dolomite, SEM image. (d) 4081.74 m, image of intercrystalline pores of dolomite, SEM image. (e) 4552.35 m, image of intercrystalline pores of dolomite, SEM image. (f) 4181.96 m, image of intercrystalline dissolve pores of dolomite, SEM image.

micritic and microcrystalline dolostone (Figures 3(a) and 3(b)). In addition, the lacustrine carbonate rock also develops grainstone (granular dolostone) intergranular pores at the micron-millimeter scale, dissolved pores of saline minerals of the carbonate rock, algal limestone (dolostone) framework pores at the millimeter scale, and fractures mainly of interlayer fractures and structural fractures. The dolostone intercrystalline pores are mainly intercrystalline pores of micritic and microcrystalline dolomite. The SEM shows that the dolomite crystal has a diameter of 1–5 μm and the casting thin-section microscopy reveals that intercrystalline pores are filled by the blue organic dye and present the diffused distribution, which fails to effectively measure the pore diameter. The cross-section of the intercrystalline pore is often observed as the regular polygon or a zigzag form, as shown in the SEM, and the SEM statistics of the intercrystalline pore size show a majority from several ten nanometers to more than ten microns (Figures 3(c)–3(e)). With the help of the image area calculation software, it is summarized that the pore throat radius of 32 typical intercrystalline pores is 50–300 nm, with an average of 145.87 nm. Dolomite intercrystalline pores extensively occur in the lacustrine carbonate rock of the West Qaidam, with the porosity of intercrystalline pores ranging from 2% to 9% and concentrated within 3%–6%, and the permeability concentrated within 0.02–0.4 mD and mostly below 0.1 mD. The porosity and permeability of such intercrystalline pores are both lower than those of the other pore types. The SEM reveals the presence of oil in intercrystalline pores and also the inferior connectivity of such pores. The intercrystalline dissolved pore of dolomite is derived from the dolomite intercrystalline pore dissolved by acid fluids. It

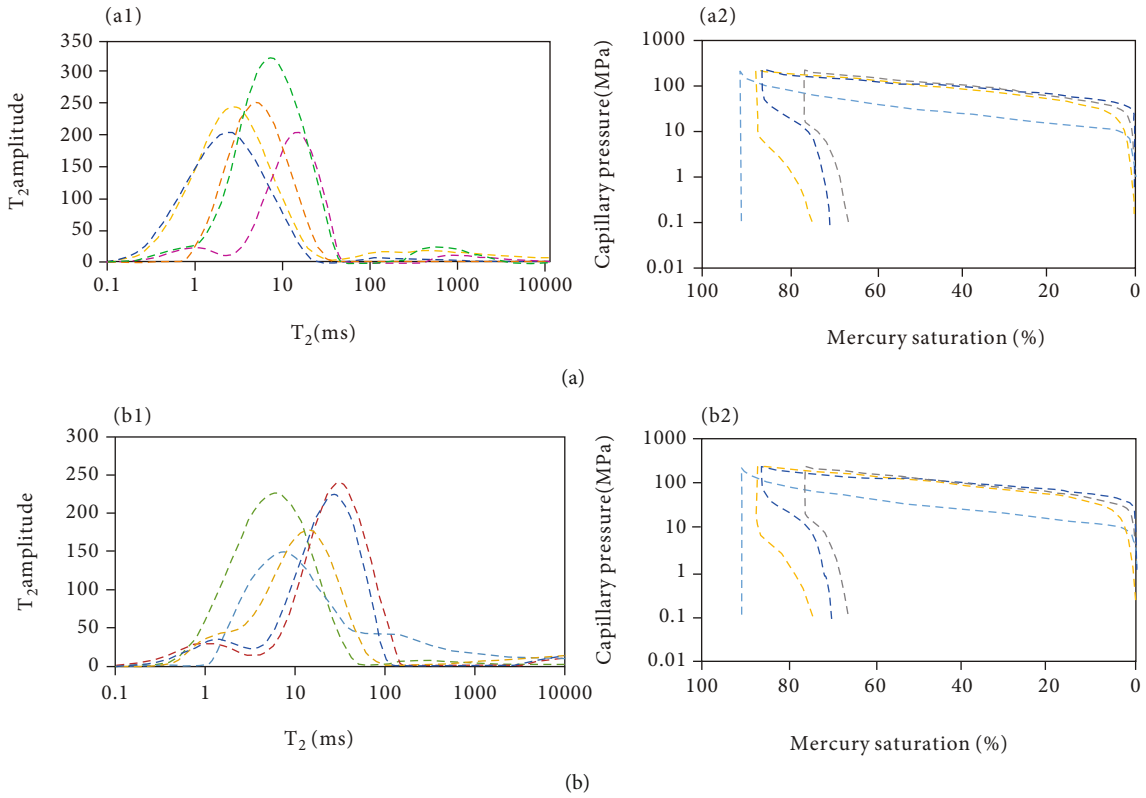

Figure 4: Pore structure of lacustrine carbonate.

presents the banded or crumby distribution and a bay-like shape under the microscope. Association of multiple intercrystalline dissolve pores is observed, and in some local areas, the zigzag cross-section of the original intercrystalline pore is maintained (Figure 3(f)). The inferior connectivity of intercrystalline pores hinders the migration of acid fluids, and thus, intercrystalline dissolved pores mainly occur on the two sides of a fracture, or around the saline mineral dissolved pore. Compared with the porosity and permeability of dolomite intercrystalline pores, those of such dissolved pores are greatly improved—the porosity is mainly 8%–14%, and the permeability is concentrated within 0.05–0.5 mD.

4.1.2. Pore Throat Size Distribution. The high-pressure mercury intrusion test results of 22 samples show that the pore throat size distribution of the samples associated with dolomite intercrystalline pores is relatively concentrated and mostly unimodal. The statistics of 5 samples demonstrate that the pore throat distribution range is mainly 0.004–0.152 μm, with the peaks occurring between 0.005 μm and 0.049 μm and averaging 0.014 μm. As revealed by the mercury intrusion statistics, the maximum pore throat radius of connected pores is 0.016–0.075 μm, with an average of 0.034 μm. The radius of pore throats contributing to 99.5% of permeability is 0.004–0.034 μm, averaging 0.012 μm. Such pores present a homogeneity coefficient of 0.602 and a structural coefficient of 0.095. The larger coefficient and lower structural coefficient imply that these pores are even in sizes with low tortuosity and close to the ideal tube bundle model of capillary tubes with identical lengths and cross-sections; hence, these pores are less modified.

For samples associated with intercrystalline dissolved pores, the pore throat size distribution is unimodal and relatively concentrated. The statistics of measured pore throats of 8 samples show that the pore throat size is mainly 0.004–0.472 μm and peaks at 0.034–0.151 μm, with an average peak pore throat radius of 0.08 μm. Compared with intercrystalline pores, intercrystalline dissolved pores are characterized by a narrower pore throat size peak range, more concentrated pore throat distribution, and a higher pore throat radius at the peak. The maximum pore throat radius of connected pores, measured by the mercury intrusion test, ranges from 0.120 μm to 0.364 μm, averaging 0.201 μm. The median pore radius (mercury saturation) is 0.036–0.187 μm, with an average of 0.088 μm. The radius range of pore throats contributing 99.5% of permeability is 0.012–0.104 μm, with an average of 0.040 μm. The homogeneity coefficient of such pores is 0.509, while the structural coefficient is 2.185. Compared with intercrystalline pores, these pores have a larger structural coefficient, suggesting higher tortuosity.

4.1.3. Pore Structure. The pore structure and pore connectivity of samples are investigated using the NMR T_2 spectrum and mercury intrusion curve, respectively [34, 43–45]. The NMR T_2 relaxation time spectrum of the samples with well-developed intercrystalline pores is found with a narrow unimodal distribution with a left-sided peak. The relaxation time at the peak ranges from 2.23 to 13.89 ms, with an average of 6.03 ms, and the signal intensity at the peak is 204.34–323.43 n/a, averaging 246.42 n/a (Figure 4(a1)). This pore

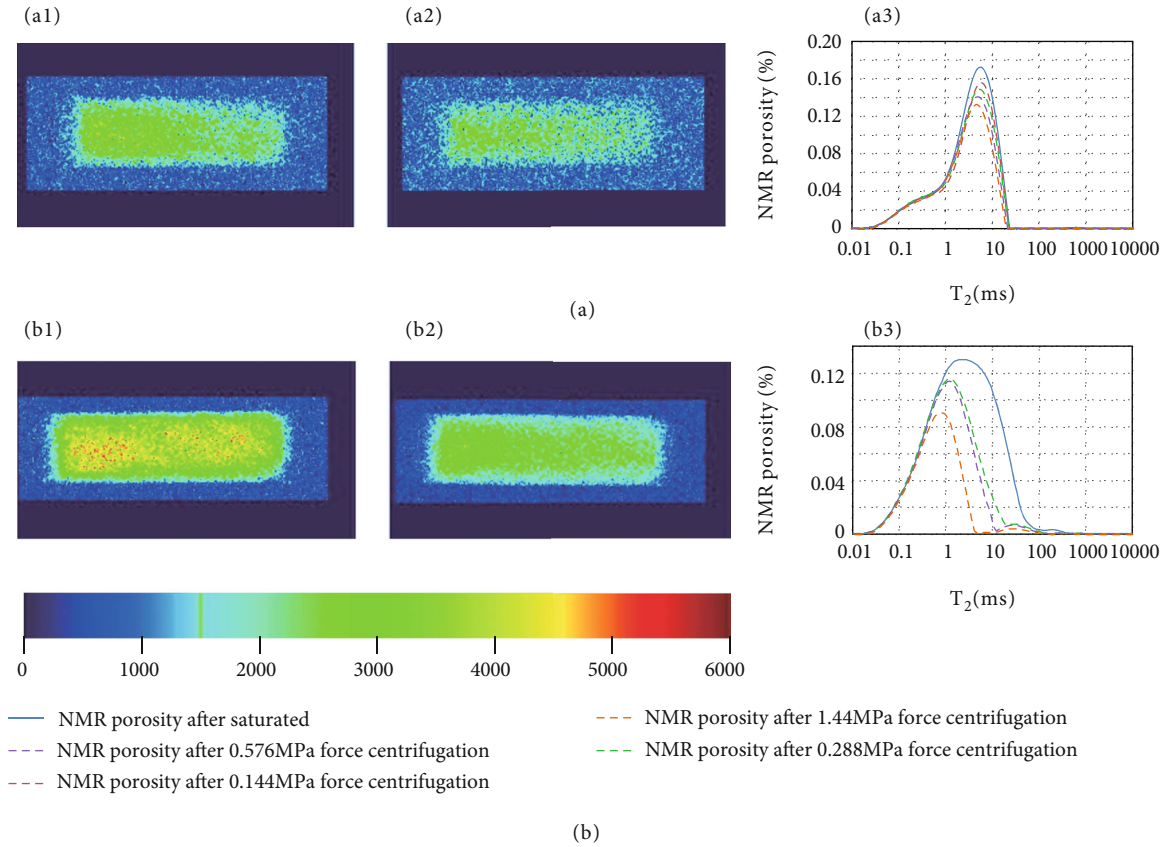

Figure 5: Fluid distribution characteristics during centrifugal process.

type shows high bond water saturations, ranging from 89.5% to 95.53% and averaging 93.08%. The mercury intrusion curve of the samples associated with intercrystalline pores is characterized by the left-skewed shape, long curve plateau, and good sorting (Figure 4(a2)). In terms of the pore structure parameters, the maximum mercury saturation is 76.14%–91.02%, averaging 83.38%; the mercury withdrawal efficiency is 0–18.38%, averaging 9.42%; the displacement pressure is 29.05–46.90 MPa, averaging 29.05 MPa; the sorting efficient is 0.63–1.25, averaging 0.93; the skewness ranges from -3.40 to 0.29, with an average of -1.32.

For the samples associated with intercrystalline dissolved pores, the NMR T_2 spectrum presents the unimodal distribution with a left-sided peak. The relaxation time at the peak ranges from 5.76 ms to 28.86 ms, averaging 16.77 ms, and the signal intensity at the peak is 149.44–242.7 n/a, with an average of 204.48 n/a. Such pores are associated with relatively higher bond water saturations (67.81%–96.32%, averaging 75.93%) (Figure 4(b1)). The mercury injection curve of these samples is characterized by the left-skewed shape, no notable plateau, and medium sorting (Figure 4(b2)). In terms of the pore structure parameters, the maximum mercury saturation is 83.50%–93.50%, averaging 86.20%; the mercury withdrawal efficiency, 4.82%–45.16%, with an average of 28.6%; the displacement pressure, 2.02–6.10 MPa, averaging 4.19 MPa; the sorting coefficient, 0.47–1.65, average 0.82; the skewness from -0.55 to 1.67, with an average of 0.43.

4.2. Occurrence Characteristics of Pore Fluids and the Threshold Pore Throat Size for Movable Fluids

4.2.1. Overall Occurrence Characteristics of Pore Fluids. The NMR imaging of the saturated sample that develops intercrystalline pores illustrates the areal distribution of fluids. The saturation fluid in the pseudocolor image appears to be green. The amount of the saturation fluid is relatively low, and yet, the fluid still presents the areal distribution after the centrifuging at the highest rotation speed—the removed fluids are small (Figure 5(a1)). The NMR relaxation time spectrum is found with only a minor shape variation during the repeated centrifuging—the relaxation time at the peak remains almost the same and the shrinkage of the relaxation time spectrum envelope is close for each centrifuging (Figure 5(a2)). For the sample associated with intercrystalline dissolved pores, it also features the overall areal distribution of fluids after saturation, as illustrated by the NMR imaging. Some local positions with higher fluid content appear to the orange red-orange in the pseudocolor image and these fluids are displaced out during centrifuging, as the postcentrifuging NMR image appears to be blue-green on an overall basis (Figure 5(b1)). The NMR relaxation time spectrum is found with considerable variation after centrifuging. The peak of the relaxation time spectrum shifts from 1 to 10 ms before centrifuging to about 1 ms after centrifuging, and the envelope area of the relaxation time spectrum changes greatly during the centrifuging treatment

corresponding to the centrifugal forces of 0.288 MPa and 1.44 MPa, respectively (Figure 5(b2)).

4.2.2. Variation Characteristics of the NMR Fluid Porosity Component during Centrifuging. The NMR porosity components of each relaxation time range after fluid saturation and during the centrifuging treatment are summarized. The NMR porosity component stands for the volumetric fraction of pores occupied by the formation water. Hence, the variation of the NMR porosity component during the centrifuging treatment implies the relative proportions of fluids stored in pore throats of varied sizes and the main storage pore throat range of movable fluids during the displacing migration. The relaxation time is positively correlated with the pore throat radius. Specifically, the relaxation time smaller than 1 ms represents micropores; that between 1 ms and 10 ms corresponds to small pores; that of 10–100 ms stands for medium pores; and that above 100 ms suggests large pores.

The porosity component variation of the samples during the centrifuging treatment is summarized and analyzed. As for the samples associated with intercrystalline pores, the precentrifuging fluid distribution mainly lies between 0.1 ms and 10 ms (the porosity component of this interval accounts for 83.5% of the total). As the centrifuging intensity grows during the treatment, fluids are continuously displaced out from pores, and yet, the NMR porosity variation magnitude for each centrifuging is consistent. The 1–10 ms interval is associated with the highest NMR porosity variation after centrifuging, followed by that of the 10–100 ms interval. Regarding the variation rate of the NMR porosity component before and after centrifuging, the highest rate is found at the relaxation time interval of 1–100 ms (up to 46.359%). The porosity component of the samples with intercrystalline pores presents a variation of 2.80% after centrifuging, corresponding to a porosity component variation rate of 28.49%, compared with that before centrifuging (Table 1).

For the samples found with the development of intercrystalline dissolved pores, the precentrifuging NMR fluid porosity component mainly lies between 0.1 ms and 10 ms and the NMR porosity component of the 1–10 ms interval possesses the highest proportions (50.81%). The NMR porosity component variation is the highest in the case of centrifuging with the centrifugal force of 0.144 MP and the largest NMR fluid porosity decline through the whole centrifuging treatment is found in the 1–10 ms interval (accounting for 75.2% of the total decline). Concerning the NMR porosity component variation rate after centrifuging, the relaxation time interval with the highest variation rate (87.87%) is 10–100 ms. The porosity component of the sample with intercrystalline dissolved pores changes by 4.33%, corresponding to a variable rate of 57.81%, compared with the precentrifuging value (Table 2).

4.2.3. The Threshold Pore Throat Radius for the Occurrence of Movable Fluids. The threshold pore throat radius range for movable fluids of 9 samples is determined using the method presented above. The computed threshold pore throat radius is 47–510 nm, with an average of 117 nm (Table 3), which is consistent with the pore throat radius range measured by the mercury intrusion test and SEM imaging statistics. Furthermore, the threshold pore throat radius of movable fluids is concentrated within 47–68 nm, which complies with the observations of the thin-section analysis and SEM. The samples with the threshold pore throat radius within this range mainly develop dolomite intercrystalline pores and the samples with the development of isolated intercrystalline pores feature smaller threshold pore throat radii, while those developing assembled intercrystalline pores have larger threshold pore throat radii. The other samples with threshold pore throat radii approaching or above 100 nm are seen with gypsum salt dissolved pores and fractures coexisting with dolomite, in addition to intercrystalline pores.

5. Discussion

5.1. Evaluation of Storage Capacity of Dolomite Intercrystalline Pores. Intercrystalline pores and intercrystalline dissolved pores are nano-micropore throats with unimodal distribution and negative skewness. The NMR T_2 spectrum of the saturated core sample is converted into the pore throat radius distribution using the conversion equation ($r = C^* T_2$). The results show that the pore size of the tight lacustrine carbonate of the lower Ganchaigou Formation lies between 50 nm and 1000 nm, mostly within 50–300 nm. Pores are found mainly with a radius of ≤100 nm, which account for 84% of total pores on an average basis. The NMR T_2 spectra of the samples associated with intercrystalline pores and intercrystalline dissolved pores are both left-skewed and represent the narrow unimodal distribution. The capillary pressure curves of such samples are characterized by a high plateau and negative skewness. The displacement pressure of two types of the pore is mostly above 3 MPa, with mercury withdrawal efficiency often below 20%. The sample with intercrystalline dissolved pores present slightly higher mercury saturations than those of the samples with intercrystalline pores, and yet, their sorting coefficients are similar. Moreover, compared with the samples associated with intercrystalline pores, those with well-developed intercrystalline dissolved pores present considerably lower displacement pressure and greatly higher withdrawal efficiency. Therefore, it is summarized that compared with intercrystalline pores, intercrystalline dissolved pores have more large pores and higher storage capacity and connectivity. The NMR porosity of the two sample types is like each other. Nonetheless, the sample with intercrystalline dissolved pores is found with higher NMR permeability and lower bond fluid saturations.

The NMR test results of fluid saturations of saturated samples are presented in Table 4. The tested samples generally have high bond fluid saturations (averaging 83.6%). Commonly, it is believed that a negative correlation exists between porosity and bond fluid saturations, and the porosity corresponding to the bond fluid saturation of 80% is used as the threshold porosity to determine reservoir effectiveness. Nevertheless, our tests suggest no considerable

Table 2: Variation of porosity component during NMR centrifugal process.

Sample	Pore type	Centrifugal force (MPa)	NMR porosity component (%)				
			0.01 ms-0.1 ms	0.1 ms-1 ms	1 ms-10 ms	10 ms-100 ms	>100 ms
24		Before centrifugation	0.179	1.089	4.191	0.857	0.008
24		0.144	0.179	1.089	3.743	0.833	0.008
24	Intercrystalline pore	0.288	0.171	1.087	3.651	0.673	0.008
24		0.576	0.166	1.055	3.567	0.529	0.007
24		1.44	0.165	1.054	3.413	0.460	0.007
	Variation of porosity component		0.014	0.035	0.779	0.397	0.001
26		Before centrifugation	0.005	1.825	11.479	0.000	0.000
26		0.144	0.001	1.727	10.407	0.000	0.000
26	Intercrystalline pore	0.288	0.000	1.550	9.812	0.000	0.000
26		0.576	0.000	1.439	8.538	0.000	0.000
26		1.44	0.000	1.421	7.504	0.000	0.000
	Variation of porosity component		0.005	0.405	3.975	0.000	0.000
S12		Before centrifugation	0.267	1.739	4.336	0.477	0.061
S12		0.144	0.262	1.738	2.207	0.062	0.034
S12	Intercrystalline dissolved pore	0.288	0.261	1.655	1.403	0.084	0.034
S12		0.576	0.259	1.589	1.030	0.080	0.032
S12		1.44	0.256	1.560	0.893	0.079	0.032
	Variation of porosity component		0.011	0.179	3.443	0.398	0.029
27		Before centrifugation	0.244	2.433	4.102	1.312	0.000
27		0.144	0.244	2.407	3.151	1.183	0.000
27	Intercrystalline dissolved pore	0.288	0.239	2.367	2.626	0.275	0.000
27		0.576	0.231	2.290	2.230	0.141	0.000
27		1.44	0.225	2.139	1.056	0.101	0.000
	Variation of porosity component		0.019	0.295	3.047	1.211	0.000

Table 3: The threshold pore throat radius of movable fluids.

Sample	Well	Median radius (nm)	The threshold pore throat radius of movable fluids (nm)
T5	S38-2	24	47
T9	S38-2	21	68
T17	S41-6-1	22	54
T19	S41-6-1	39	103
T20	S43	10	58
TS7	S52-1	89	96
TS12	S52-1	51	64
TS19	S52-1	14	52
TS21	S52-1	110	510

correlation between the bond fluid saturation and porosity. This can be explained below. Porosity represents the overall storage capacity of samples, while the bond fluid saturation stands for the proportions of bond fluids. The bond fluid saturation grows with the increasing proportions of isolated pore throats. Furthermore, a high positive correlation is identified in this research between the ratio of the postcentrifuging NMR porosity to the postsaturation NMR porosity and bond fluid saturation. Therefore, this ratio can be used to evaluate the pore effectiveness and pores are considered effective with the postcentrifuging/postsaturation NMR porosity ratio below 0.55, which corresponds to the bond fluid saturation lower than 80%. The lacustrine carbonate rock with the development of dolomite intercrystalline pores is generally found with a certain storage capacity. Its pore distribution is relatively concentrated, while the pore connectivity is low. Analyzing the proportions of movable fluids that can effectively flow in pores is key to evaluating the effectiveness of dolomite intercrystalline pores.

5.2. Occurrence Characteristics of Movable Fluids and Corresponding Influential Factors. Fluids in samples associated with intercrystalline pores mostly occur in micros (with a relaxation time < 1 ms) and small pores (with a relaxation time of 1–10 ms), which account for 94.7% of the NMR fluid porosity component. Moreover, movable fluids (that can be displaced by centrifuging) are primarily stored in small (with a relaxation time of 1–10 ms) and medium pores (with a relaxation time of 10–100 ms). For samples with development of intercrystalline dissolved pores, fluids mainly occur in micro and small pores (accounting for 84.23% of the NMR fluid porosity). Small pores provide the main accommodation for fluids, while compared with intercrystalline pores, intercrystalline dissolved pores present higher

Table 4: The NMR test results of samples.

Sample	Well	Depth (m)	NMR porosity (%)	NMR permeability (10^{-3} μm^2)	T_2 cutoff value (ms)	Bound water saturation (%)	NMR porosity after centrifuged by 1.44 MPa centrifugal force (%)	Porosity after saturated/porosity after centrifugation
T5	S38-2	3504.0	9.39	0.04	2.60	85.10	6.15	0.65
T9	S38-2	3510.9	7.18	0.02	3.70	93.60	5.50	0.77
T17	S41-6-1	3855.4	8.41	0.16	2.80	91.80	5.35	0.64
T19	S41-6-1	3867.9	8.96	0.06	8.40	97.70	6.88	0.77
T20	S43-1	3920.6	5.70	0.06	1.80	66.10	3.15	0.55
TS7	S52-1	4543.6	10.35	0.46	13.60	89.40	6.12	0.59
TS12	S52-1	4550.1	6.85	0.38	6.40	83.20	2.85	0.42
TS19	S52-1	4553.9	8.20	0.08	6.90	88.30	5.63	0.69
TS21	S52-1	4554.4	10.49	2.39	25.50	56.86	4.35	0.41

proportions of fluids stored in medium pores. Movable fluids (that can be displaced out by centrifuging) mostly occur in small and medium pores. During the centrifuging treatment, gentle centrifuging can result in a large variation of the porosity component. The connectivity of intercrystalline dissolved pores is higher than that of intercrystalline pores and the movable fluid proportions are also higher (Table 4). The distribution ranges of the NMR relaxation time are consistent between the intercrystalline pores and intercrystalline dissolved pores. However, a higher variable rate of the porosity component after centrifuging is presented by intercrystalline dissolved pores, compared with that of intercrystalline pores—the pore connectivity of the sample with intercrystalline dissolved pores is considerably higher.

The proportions of stored movable fluids in samples are dependent on the pore type, pore throat distribution, pore structure, and contact surface property [46–48]. The tested samples are observed with extensive development of dolomite intercrystalline pores and intercrystalline dissolved pores. In addition, some samples also present dissolved pores of saline minerals and fractures and such samples are observed with higher pore connectivity and larger proportions of movable fluids, compared with samples with dolomite intercrystalline pores. The samples associated with dolomite intercrystalline pores are all ultralow porosity and ultralow permeability. The fluid seepage through such samples does not comply with Darcy's law, and the nonlinear flow and threshold flow pressure are present. The threshold pressure for flow is negatively correlated with movable fluid proportions and is also closely related to the surface property and pore structure. The rock composition of samples is dominated by micritic carbonates and clay minerals, and the pore surface is hydrophilic (with contact angles of 40°–60°). With the hydrophilic pore surface, movable fluids typically occur in larger pores and centers of tiny pores, and the proportions of surface bond fluids are high. Besides, the pore structure differentiation also greatly affects the occurrence of movable fluids. For example, samples T19 and TS7 tested in our research are found with greatly varied movable fluid saturations (the movable fluid saturation of T19 amounts to 2.3%, while that of TS7 is 10.6%). The capillary pressure curves and pore throat radius distribution curve were measured in the mercury intrusion test of two samples, and it is revealed that compared with Sample T19, Sample TS7 presents the positive skewness of pore throats, low displacement pressure, high mercury saturation, and high mercury withdrawal efficiency (Figure 6). Therefore, it is safe to say that samples with coarser pore throats and higher proportions of connected pore throats are associated with higher proportions of movable fluids.

The type and content of minerals are important factors affecting fluid occurrence characteristics and movable fluid saturation. The vertical variation characteristics of mineral content, gas porosity, NMR porosity, and movable fluid saturation reflect the influence of mineral content on the storage space and fluid saturation. The longitudinal variation rule of terrigenous debris (quartz+feldspar) contents is consistent with the variation rule of clay mineral contents. The longitudinal variation rule of carbonate is opposite to that of terrigenous debris (Figure 7).

The gas porosity and the NMR porosity have the same changing laws, both of which reflect the storage capacity of the samples, and the NMR porosity reflects the relative content of the saturated fluids. Movable fluids saturation reflects the proportion of movable fluids and the connectivity of pore throats; the higher the movable fluid saturation, the better the connectivity of the pores. The geometric mean of the NMR relaxation time reflects the concentration of the pore throat distribution of the sample. The larger the geometric mean, the more concentrated the pore throat distribution. Longitudinal NMR porosity is mainly distributed in 3-9%, up to 15%.

The variation law of longitudinal NMR porosity is consistent with the change of carbonate. The higher NMR porosity corresponds to the higher carbonate and the lower terrigenous debris and clay. The samples with higher carbonate have more dolomite intercrystalline pores, and the fluid saturation is higher. The dolomite intercrystalline pores are the main space for fluid occurrence.

Comparing the NMR relaxation spectra of S1 and S2 samples, the NMR porosity and movable fluid saturation of S2 are higher than those of S1. The NMR porosity of the S2 sample is 14.91%, and the movable fluid saturation is 44.22%. The NMR porosity of the S1 sample is 10.71%, and the movable fluid saturation is 30.72%. Comparing the

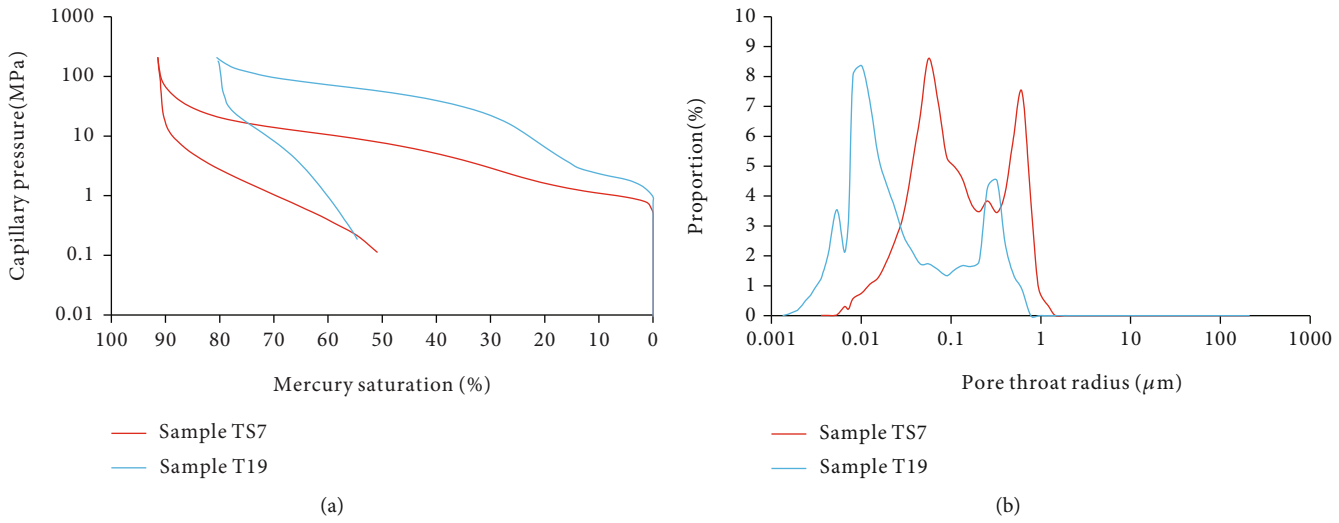

Figure 6: Mercury intrusion capillary pressure curve and pore throat radius distribution curve.

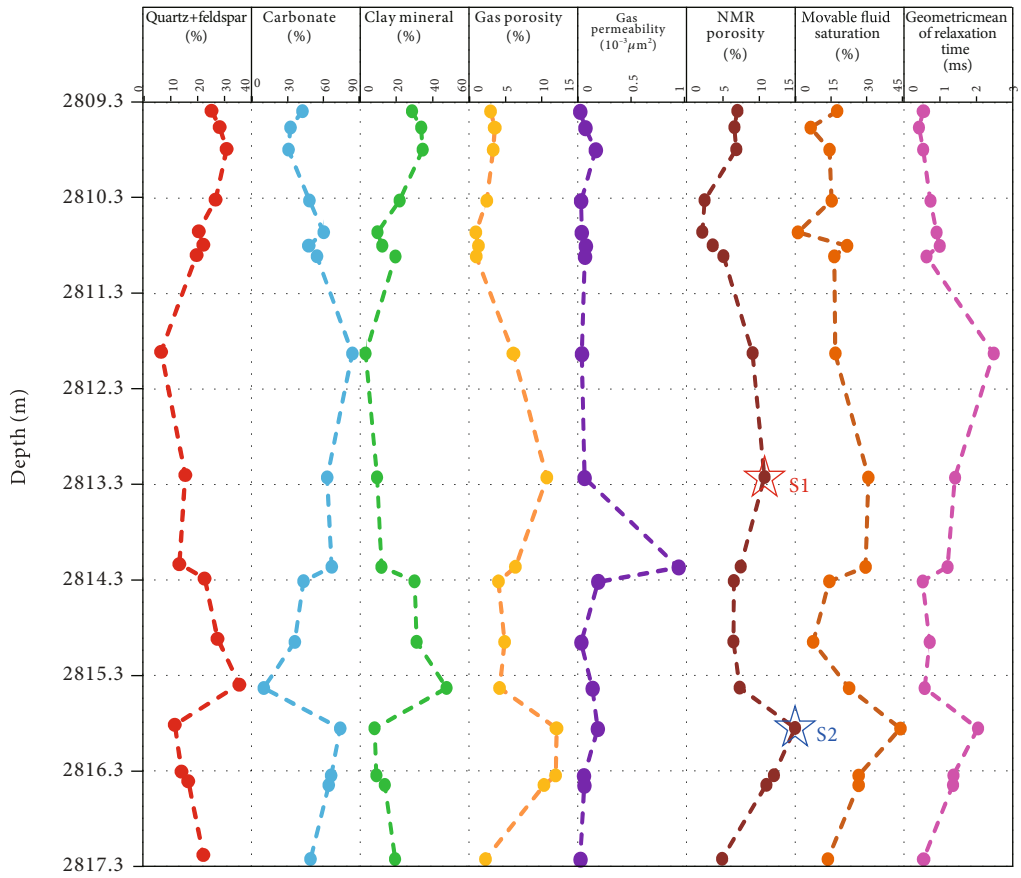

Figure 7: Longitudinal variation characteristics of sample mineral content and NMR parameters.

NMR relaxation spectra of the two samples, it is found that the relaxation spectra of the two samples are unimodal distribution, and the pore types of the two samples are dolomite intercrystalline pores, but the NMR spectrum of the S2 sample has a higher peak. The distribution is more concentrated, and the change in the cumulative value of NMR porosity before and after centrifugation of the S2 sample is also larger, which all reflect that the fluid saturation and pore connectivity of the S2 sample are better (Figure 8). The reason for the above difference is that the carbonate of the S2 is relatively high, and the dolomite intercrystalline pores are more developed in S2.

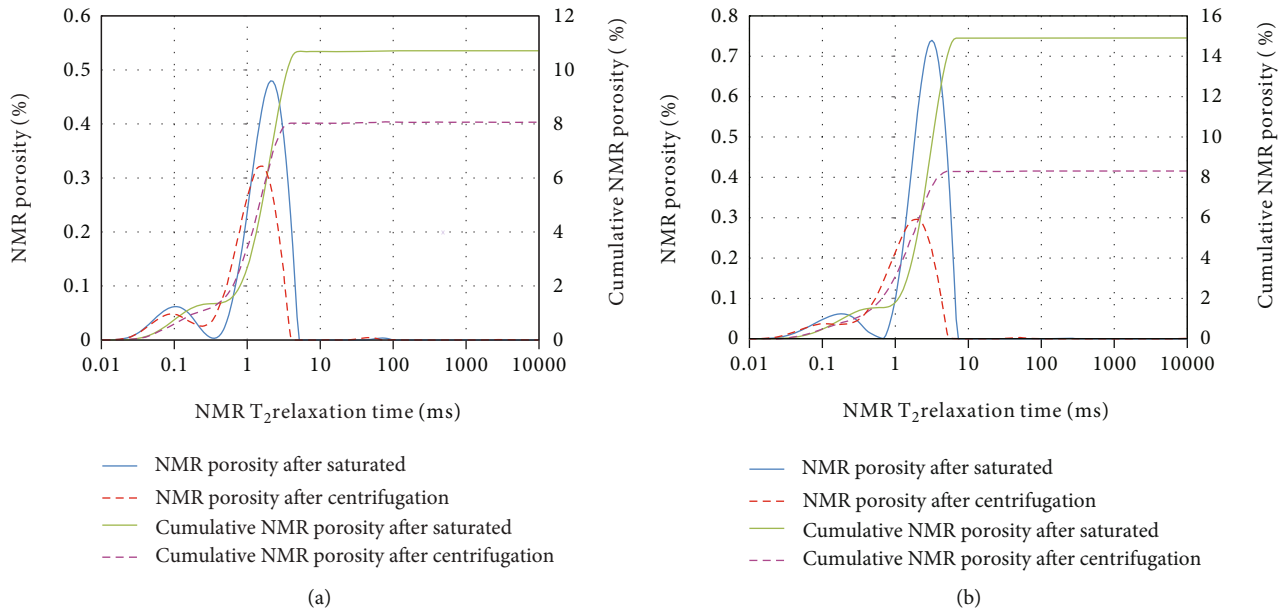

Figure 8: NMR relaxation spectrum. (a) NMR relaxation spectrum of sample S1. (b) NMR relaxation spectrum of sample S2.

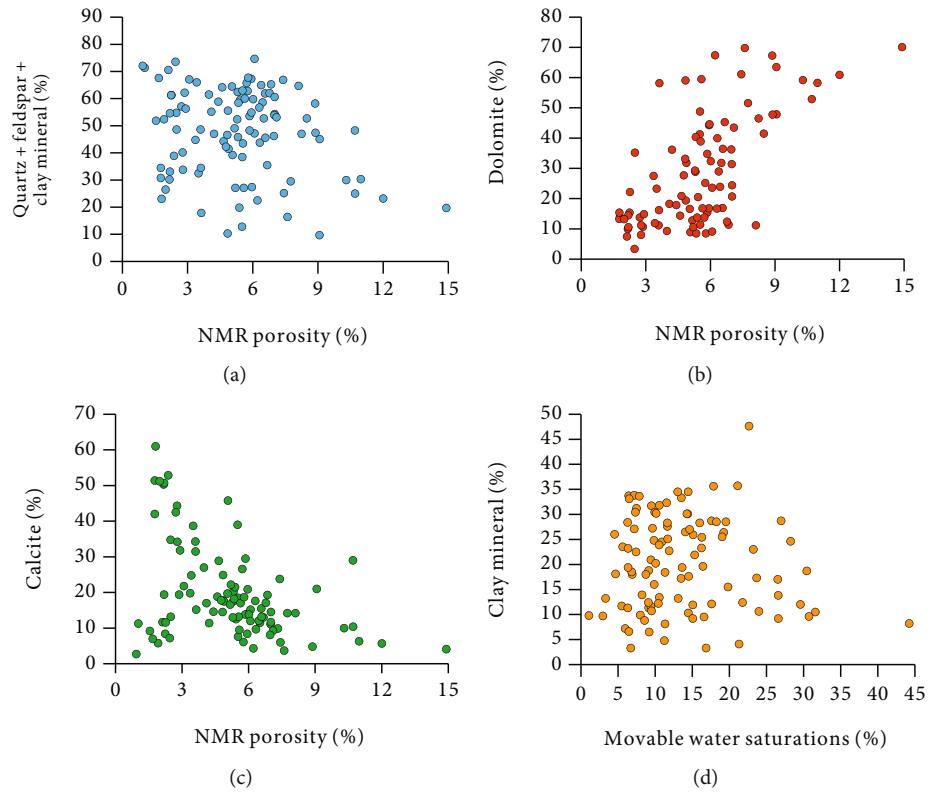

Figure 9: Scatter diagram of mineral composition versus NMR porosity and movable water saturations.

Mineral content is an important factor affecting the fluid occurrence characteristics in microscopic pores. Differences in mineral morphology and physical properties result in differences in the degree of pore development and wettability, as well as differences in fluid saturation.

In this study, the correlation between the mineral content of the sample and the NMR porosity and movable fluid saturation was analyzed. The analysis shows that there is a negative correlation between the content of terrigenous debris and the nuclear magnetic porosity, which is because

the particle size of clasts in the samples is finer than that of silt, and the intergranular pores of silt-grade particles are not developed. The higher the content of clastic particles, the denser the sample, and the lower the NMR porosity. The content of dolomite has an obvious positive correlation with NMR porosity. The higher the content of dolomite, the more developed the intercrystalline pores, the better the storage capacity of the sample, and the higher the relative proportion of saturated fluid. The calcite content is negatively correlated with the nuclear magnetic porosity. The calcite does not develop intercrystalline pores. The higher the calcite, the denser the sample. There is a negative correlation between the clay minerals in the sample and the movable fluid saturation. On the one hand, the clay minerals have the effect of blocking the pores, resulting in the reduction of the pore space and the decrease of the movable fluid. On the other hand, clay minerals are easily combined with fluids to become bound fluids, resulting in a decrease in the saturation of movable fluids (Figure 9).

6. Conclusions

(1) For the lacustrine carbonate reservoir of the lower Ganchaigou Formation in the West Qaidam, which features the development of dolomite intercrystalline pores, the gas porosity is 2%–14% and the permeability is 0.02–0.5 mD, representing the ultralow-porosity and ultralow-permeability reservoir. Dolomite intercrystalline pores are the main pore type of reservoir. These pores are nano-micropores, mostly presenting triangle, zigzag, and regular polygon cross-section shapes. The pore throat radius distribution range measured by the SEM is 50–300 nm. Intercrystalline dissolved pores are formed by acid erosion of intercrystalline pores

(2) Intercrystalline pores and intercrystalline dissolved pores are found with the left-skewed unimodal size distribution. Their capillary pressure curves are characterized by a high plateau and negative skewness. The NMR relaxation time spectra are left-skewed and imply higher bond water saturations. Compared with intercrystalline pores, intercrystalline dissolved pores have more large pores, and lower bond water saturations, associated with higher storage capacity and connectivity

(3) For samples with intercrystalline pores, the relaxation time interval found with higher variation rates of the NMR porosity component of movable fluids is 1–10 ms; for samples with intercrystalline dissolved pores, that is, 1–100 ms. During the centrifuging treatment, the largest porosity component variation occurs in small and medium pores, which are the main distribution space of movable fluids

(4) The pore throat fluid distribution is investigated via the NMR tests of samples that are first saturated and then put through multiple centrifuging treatments. Moreover, the threshold pore throat radius for movable fluids is determined according to the separation point between movable and bond fluids. The movable fluid threshold pore throat radius of the tested samples is 47 nm

(5) The relative proportion of movable fluids stored in samples is dependent on the pore type, pore throat size distribution, pore structure, and contact surface property. In samples that develop dolomite intercrystalline pores, the fluid seepage does not comply with Darcy's law, due to the lower permeability. The threshold pressure of fluid flow grows, with the decreasing proportions of movable fluids. The sample is hydrophilic and movable fluids mainly occur in the centers of pores. The samples with higher proportions of coarse pores and connectivity have higher proportions of movable fluids

Data Availability

Data would be available on request.

Conflicts of Interest

The authors declare that they have no conflicts of interest.

Acknowledgments

This research was funded by the National Natural Science Foundation of China, No. 42172169.

References

[1] Y. Weipeng, Y. Tao, L. Xin, H. Fuxi, W. Xiaozhi, and T. Hui, "Geological characteristics and hydrocarbon exploration potential of lacustrine carbonate rock in China," *China Petroleum Exploration*, vol. 19, no. 4, pp. 11–17, 2014.

[2] Z. Caineng, Y. Zhi, T. Shizhen et al., "Nano-hydrocarbon and the accumulation in coexisting source and reservoir," *Petroleum Exploration and Development*, vol. 39, no. 1, pp. 15–32, 2012.

[3] M. A. Bustillo, M. E. Arribas, and M. Bustillo, "Dolomitization and silicification in low-energy lacustrine carbonates (Paleogene, Madrid Basin, Spain)," *Sedimentary Geology*, vol. 151, no. 1-2, pp. 107–126, 2002.

[4] A. S. Cohen and C. Thouin, "Nearshore carbonate deposits in lake Tanganyika," *Geology*, vol. 15, no. 5, pp. 414–418, 1987.

[5] M. E. Tueher and V. P. Wright, *Carbonate Sedimentology*, Black well Scientific Publications, Oxford, 1990.

[6] L. Kuang, T. A. Yong, L. E. Dewen et al., "Formation conditions and exploration potential of tight oil in the Permian saline lacustrine dolomitic rock, Junggar Basin, NW China," *Petroleum Exploration and Development*, vol. 39, no. 6, pp. 700–711, 2012.

[7] H. G. Machel, "Concepts and models of dolomitization: a critical reappraisal," *Geological Society of London Special Publication*, vol. 235, no. 1, pp. 7–63, 2004.

[8] G. Wahlman, "Reflux dolomite crystal size variation in cyclic inner ramp reservoir facies, bromide formation (Ordovician), Arkoma Basin, Southeastern Oklahoma," *The Sedimentary Record*, vol. 8, no. 3, pp. 4–9, 2010.

[9] D. Ren, L. Ma, D. Liu, J. Tao, X. Liu, and R. Zhang, "Control mechanism and parameter simulation of oil-water properties on spontaneous imbibition efficiency of tight sandstone reservoir," *Frontiers in Physics*, vol. 10, no. 10, 2022.

[10] F. Gao, Y. Zhang, X. Pu, Y. Yang, and Z. Zhang, "Type of dolomization and formation mechanismpp. A case study of Palaeogene Es1 in Qikou Sag," *Journal of Jilin University (Earth Science Edition)*, vol. 47, no. 2, pp. 355–369, 2017.

[11] C. Seard, G. Camoin, J. M. Rouchy, and A. Virgone, "Composition, structure and evolution of a lacustrine carbonate margin dominated by microbialites: case study from the Green River formation (Eocene; Wyoming, USA)," *Palaeogeography Palaeoclimatology Palaeoecology*, vol. 381-382, pp. 128–144, 2013.

[12] L. L. Mao, H. S. Yi, C. J. Ji, and G. Xia, "Petrography and carbon-oxygen isotope characteristics of the Cenozoic lacustrine carbonate rocks in Qaidam Basin," *Geological Science and Technology Information*, vol. 33, no. 1, pp. 41–48, 2014.

[13] C. W. Qu, C. M. Lin, M. J. Cai, Y. Z. Cheng, B. J. Wang, and X. Zhang, "Characteristics of dolostone reservoir in Sha 3 Group from Palaeogene Shahejie Formation in Beitang Sag, Bohaiwan Basin," *Acta Geologica Sinica*, vol. 88, no. 8, pp. 1588–1602, 2014.

[14] S. T. Fu, D. W. Zhang, J. Q. Xue, and X. B. Zhang, "Exploration potential and geological conditions of tight oil in the Qaidam Basin," *Acta Sedimentologica Sinica*, vol. 31, no. 4, pp. 672–682, 2013.

[15] Z. Q. Guo, J. H. Zhong, W. H. Liu, Z. F. Wen, Z. H. Liu, and H. Q. Wang, "Reservoir characteristics and significance of tertiary lacustrain reef in Western Qaidam," *Acta Sedimentologica Sinica*, vol. 22, no. 3, pp. 425–433, 2004.

[16] J. Wang, D. Zhang, Y. Shi et al., "Salt lake depositional characteristics of upper member of lower Ganchaigou formation, Western Qaidam basin," *Journal of Jilin University (Earth Science Edition)*, vol. 50, no. 2, pp. 442–453, 2020.

[17] Z. H. Shiming, Z. H. Xiaojun, Z. H. Tingjing, W. A. Pu, N. A. Xixiang, and G. O. Yingchun, "Reservoir characteristics of the Paleogene mixed carbonate-siliciclastic rock or succession and its influencing factors in the Shizigou area of the Western Qaidam Basin," *Geoscience*, vol. 31, no. 5, pp. 1059–1068, 2017.

[18] J. E. Hargrave, M. K. Hicks, and C. A. Scholz, "Lacustrine carbonates from Lake Turkana, Kenya: a depositional model of carbonates in an extensional basin," *Journal of Sedimentary Research*, vol. 84, no. 3, pp. 224–237, 2014.

[19] L. I. Zhanguo, Z. H. Chao, L. I. Senming et al., "Geological features and exploration fields of tight oil in the Cenozoic of western Qaidam Basin, NW China," *Petroleum Exploration and Development*, vol. 44, no. 2, pp. 217–225, 2017.

[20] J. Wang, D. Zhang, S. Yang et al., "Sedimentary characteristics and genesis of the salt lake with the upper member of the Lower Ganchaigou Formation from Yingxi sag, Qaidam basin," *Marine and Petroleum Geology*, vol. 111, pp. 135–155, 2020.

[21] W. Zhang, X. Jian, L. Fu, F. Feng, and P. Guan, "Reservoir characterization and hydrocarbon accumulation in late Cenozoic lacustrine mixed carbonate-siliciclastic fine-grained deposits of the northwestern Qaidam basin, NW China," *Marine and Petroleum Geology*, vol. 98, pp. 675–686, 2018.

[22] W. U. Kunyu, L. I. Chun, L. I. Xiang et al., "Geological characteristics of hydrocarbon pool in Yingxiongling Structural Zone, Qaidam Basin," *Geoscience*, vol. 34, no. 2, pp. 378–389, 2020.

[23] Y. Xiong, X. Tan, K. Wu, Q. Xu, Y. Liu, and Y. Qiao, "Petrogenesis of the Eocene lacustrine evaporites in the western Qaidam Basin: implications for regional tectonic and climate changes," *Sedimentary Geology*, vol. 416, article 105867, 2021.

[24] F. Cheng, M. Jolivet, Z. Guo, L. Wang, C. Zhang, and X. Li, "Cenozoic evolution of the Qaidam basin and implications for the growth of the northern Tibetan plateau: a review," *Earth-Science Reviews*, vol. 220, article 103730, 2021.

[25] H. Chenggang, Y. Jianying, and T. Guangrong, "The geochemical characteristics and formation mechanism of the Eocene lacustrine dolomite reservoirs in the western Qaidam," *Earth Science Frontiers*, vol. 23, no. 3, pp. 230–242, 2016.

[26] J. Yuan, C. Huang, Z. Cao et al., "Carbon and oxygen isotopic composition of saline lacustrine dolomite and its palaeoenvironmental significance: a case study of Lower Eocene Ganchaigou formation in western Qaidam Basin," *Geochimica*, vol. 44, no. 3, pp. 254–266, 2015.

[27] M. Zha, Y. Su, C. Gao, X. Qu, X. Wang, and X. Ding, "Tight reservoir space characteristics and controlling factorspp. An example from Permian Lucaogou formation in Jimsar sag, Juggar basin, Northwest China," *Journal of China University of Mining & Technology*, vol. 46, no. 1, pp. 85–93, 2017.

[28] D. E. Kun, Z. H. Wen, Z. H. Lifa et al., "Influencing factors of micropores in the graptolite shale of Ordovician Pingliang Formation in Ordos Basin, NW China," *Petroleum Exploration and Development*, vol. 43, no. 3, pp. 416–424, 2016.

[29] W. A. Minglei, F. Zhang, L. I. Yuting et al., "Quantitative research on tight oil microscopic state of Chang 7 Member of Triassic Yanchang Formation in Ordos Basin, NW China," *Petroleum Exploration and Development*, vol. 42, no. 6, pp. 827–832, 2015.

[30] T. Fang, L. Zhang, N. Liu et al., "Quantitative characterization of pore structure of tight gas sandstone reserviors by NMR T_2 spectrum technologypp. A case study of carboniferous-Permian tight sand stone reservoir in Linqing depression," *Acta Petrolei Sinica*, vol. 38, no. 8, pp. 902–914, 2017.

[31] M. Wang, J. Yang, Z. Wang, and S. Lu, "Nanometer-scale pore characteristics of lacustrine shale, Songliao Basin, NE China," *PLoS One*, vol. 10, no. 8, 2015.

[32] X. Liu and X. Hu, "Progress of NMR log in evaluating reservoir pore structure in last five years," *Progress in Geophysics*, vol. 24, no. 6, pp. 2194–2201, 2009.

[33] J. Yan, D. Wen, Z. Li et al., "The quantitative evaluation method of low permeable sandstone pore structure based on nuclear magnetic resonance (NMR) loggin," *Chinese Journal of Geophysics*, vol. 59, no. 4, pp. 1543–1552, 2016.

[34] Y. Volokitin, W. J. Looyestijn, W. F. Slijkerman, and J. P. Hofman, "A practical approach to obtain primary drainage capillary pressure curves from NMR core and log data," *Petrophysics*, vol. 42, no. 4, pp. 334–343, 2001.

[35] T. Liu, S. Wang, R. Fu, M. Zhou, Y. Li, and Y. Luo, "Analysis of rock pore throat structure with NMR spectra," *Oil Geophysical Prospecting*, vol. 38, no. 3, pp. 328–333, 2003.

[36] Z. Cheng, W. Liu, S. Li et al., "High-efficiency separation of CO_2 from CO_2-CH_4 gas mixtures via gas hydrates under static conditions," *Separation and Purification Technology*, vol. 296, article 121297, 2022.

[37] H. Yun, W. Zhao, B. Liu, C. Zhou, and F. Zhou, "Researching rock pore structure with T_2 distribution," *Well Logging Technology*, vol. 26, no. 1, pp. 18–21, 2002.

[38] E. Müller-Huber, J. Schön, and F. Börner, "Pore space characterization in carbonate rocks — approach to combine nuclear magnetic resonance and elastic wave velocity measurements," *Journal of Applied Geophysics*, vol. 127, pp. 68–81, 2016.

[39] H. Zhou, F. Gao, X. Zhou, H. B. Liu, B. X. Guo, and C. S. Wang, "The translation research of different types sandstone of Yungang Grottoes in NMR T2-mercury capillary pressure," *Progress in Geophysics*, vol. 28, no. 5, pp. 2759–2766, 2013.

[40] X. Gong, H. Tang, F. Zhao, J. Wang, and H. Xiong, "Quantitative characterization of pore structure in shale reservoir of Longmaxi Formation in Sichuan Basin," *Lithologic Reservoirs*, vol. 28, no. 3, pp. 48–57, 2016.

[41] S. O. Yan, L. I. Zhuo, Z. Jiang, L. Qun, L. Dongdong, and G. Zhiye, "Progress and development trend of unconventional oil and gas geological research," *Petroleum Exploration and Development*, vol. 44, no. 4, pp. 675–685, 2017.

[42] C. Liu, Y. Liang, and K. Wang, "A numerical investigation on deep shale gas recovery," *Energy Geoscience*, vol. 2, no. 4, pp. 274–284, 2021.

[43] X. I. Dianshi, L. U. Shuangfang, L. U. Zhengyuan, W. Huang, and G. U. Meiwei, "Combining nuclear magnetic resonance and rate-controlled porosimetry to probe the pore-throat structure of tight sandstones," *Petroleum Exploration and Development*, vol. 43, no. 6, pp. 1049–1059, 2016.

[44] Z.-Q. Mao, Y.-D. He, and X.-J. Ren, "An improved method of using NMR T2Distribution to evaluate pore size distribution," *Chinese Journal of Geophysics*, vol. 48, no. 2, pp. 412–418, 2005.

[45] T. Li, Z. Li, Y. Zhao, Z. Guo, and C. Wang, "Consistency of pore structures between NMR and mercury intrusion method," *Natural Gas Industry*, vol. 26, no. 10, pp. 57–59, 2006.

[46] T. Shi, W. Sun, and S. He, "Relationship between micro-pore structure and movable fluid saturation in low permeability reservoir," *Geological Science and Technology Information*, vol. 31, no. 4, pp. 81–84, 2012.

[47] D. Khan, L. Qiu, C. Liang et al., "Formation and distribution of different pore types in the lacustrine calcareous shale: insights from XRD, FE-SEM, and low-pressure nitrogen adsorption analyses," *ACS Omega*, vol. 7, no. 12, pp. 10820–10839, 2022.

[48] Q. Li, S. Wu, X. Zhai, S. Pan, and S. Lin, "Micro/nanopore systems in lacustrine tight oil reservoirs, China," *Journal of Nanoscience and Nanotechnology*, vol. 21, no. 1, pp. 599–607, 2021.